Structure, bonding, and adhesion at the TiC(100)/Fe(110) interface from first principles

A. Arya and Emily A. Carter
Department of Chemistry and Biochemistry, University of California, Los Angeles, California 90095-1569

(Received 30 September 2002; accepted 12 February 2003)

Metal carbide ceramics offer potential as protective coatings for steels. Here we report a pseudopotential-based density functional (DFT) investigation of one such coating, wherein we predict the atomic structure, bonding, and the ideal work of adhesion (W_{ad}^{ideal}) of the interface between a TiC(100) coating and a bcc Fe(110) substrate. Calibration of the DFT approximations used yields TiC and Fe bulk properties in reasonable agreement with experiment. Subsequent characterization of the low-index TiC and Fe surfaces reveals that all surfaces retain near bulk termination, in agreement with experiment. Stabilities of both TiC and Fe surfaces increase with their packing densities, i.e., $(110)<(111)<(100)$ for TiC and $(111)<(100)<(110)$ for bcc Fe. We estimate that the minimum critical stress required for crack propagation in bcc Fe is 27% larger than that in TiC. The TiC(100)/Fe(110) interface exhibits a lattice mismatch of $\sim 2.1\%$, leading to a smooth interface with only a small structural relaxation, except for the ultrathin 1 monolayer (ML) coating. A mixture of metallic and covalent bonding dominates across the interface, due to significant C *p*-Fe *d* interaction and somewhat less pronounced Ti *d*-Fe *d* mixing; the latter is found to decrease with increasing coating thickness, but reaches a saturation value for 3-ML-thick coating. The asymptotic value of W_{ad}^{ideal} for the TiC(100)/Fe(110) interface is predicted to be ~ 2.56 J/m^2 and is reached for a 3-ML-thick coating of TiC on Fe. This interface strength is considerably smaller than the energy required for cracking TiC or Fe, but may still be strong enough to survive as a coating for steel in extreme environments. © *2003 American Institute of Physics.*
[DOI: 10.1063/1.1565323]

I. INTRODUCTION

Transition metal carbides are used for high-temperature applications in which thermal shock, wear and corrosion resistance are required.[1–4] These materials comprise structural components in automotive engines, gas turbine engines, and other machinery, as well as entering into several other aerospace and military applications.[5,6] These ceramics possess unusual combinations of physical, chemical, and mechanical properties which make them highly attractive from a technological as well as fundamental point of view. In particular, valence band photoemission, X-ray emission, and optical spectroscopic studies[1,4,5,7] reveal a a high amount of covalent bonding in combination with small band gaps or even metal-like transport properties. The multifunctional behavior of transition metal carbides result from a mixture of ionic, covalent, and metallic bonding present simultaneously in a given crystal structure.[8] High melting points, hardness, and stiffness combined with good corrosion and oxidation resistance[6,8,9] also make these carbides ideal candidates as protective coating materials under extremely harsh and corrosive environments.[10,11] Hence, during the last two decades or so, interest has shifted from properties of bulk crystals to those of their surfaces[12–14] and interfaces formed between these ceramics and metal–alloy substrates.[15,16] Metal–ceramic interfaces also appear in thermal barrier coatings, heterogeneous catalysts, microelectronics, metal processing, and tribology.[4,5,17] No wonder then that an important thrust in applied and fundamental research has been focused on understanding and optimizing the mechanical, chemical, and electrical properties of these interfaces.[18–20]

Given the wide use of steel in harsh operating environments, optimal protective coatings are desirable. The current chrome coating on ferritic steels contains inherent microcracks formed during the electrodeposition process. These cracks tend to widen under severe operating conditions, leading to diffusion of reactive gases to the base metal. This causes materials degradation via compound formation, melting, etc., thereby limiting the lifetime of the component.[6,9] These ferritic steels are used in several industrial applications,[5,6] e.g., pressure vessel and tubing, oil and gas pipe lines, transmission towers, and gun barrels. As a result, alternative coatings that can withstand high-amplitude thermal and mechanical fluctuations and can protect steel against reactive and corrosive gas environments are of considerable interest. The other desirable property of good coating is to have strong adhesion to the steels, which implies that the mechanical and thermodynamic properties of the coating material should be commensurate with those of steels. These properties include coefficients of thermal expansion, melting point, stability over a wide range of composition, hardness, and stiffness. A literature survey of several carbides, nitrides, and oxides of transition metals, in relation to that of ferritic steels,[21–24] indicates that optimal choices may include TiC, ZrC, and *c*-BN. These ceramics have several favorable properties: melting points above 3000 °C, thermal conductivities

 © 2003 American Institute of Physics

Downloaded 14 May 2003 to 128.97.45.185. Redistribution subject to AIP license or copyright, see http://ojps.aip.org/jcpo/jcpcr.jsp

much lower than that of the conventional chrome coating, coefficients of thermal expansion comparable to that of steels, and in some specific orientations, lattice mismatches with bcc Fe$\leqslant$3%; i.e., they should form coherent interfaces. Hence, these ceramics may be able to act as suitable coating materials for steels to provide wear and thermal shock resistance.

The electronic structure of bulk transition metal carbides has been studied theoretically using both cluster models[25,26] and all-electron three-dimensional (3D) periodic DFT-based methods, e.g., the augmented plane wave (APW) method,[27] muffin-tin orbital (MTO) technique,[28] and their linearized versions LAPW and LMTO.[29] Several review articles on these investigations are available.[2,3,8] The band structures obtained using APW and LAPW methods for carbides of Ti, Zr, V, and Nb compare well with photoelectron spectroscopy (PES) using X-rays (XPS) and ultraviolet radiation (UPS), as well as other spectroscopic methods,[1,4,7] e.g., electron energy loss spectroscopy (EELS) and X-ray emission specroscopy (XES). The basic conclusions are that $M-X$ bonding dominates over $M-M$ bonding and significant charge transfer from metal to nonmetal atoms occurs. We shall see that our pseudopotential-based DFT calculations agree well with above findings, where TiC is found to exhibit a mixture of covalent, ionic, and metallic bonding.

Two excellent reviews on the surfaces of transition metal carbides are available,[12,30] in which experimental and theoretical investigations of surface- and vacancy-induced states, chemical shifts, and surface shifts in core-electron binding energies, surface relaxations, and reconstructions are discussed. The low-index surfaces of these compounds give, with few exceptions, distinct 1×1 low-energy electron diffraction (LEED) patterns indicating no surface reconstructions. Chemical shifts in core-level binding energies have been utilized to investigate the extent of charge transfer in these compounds. Among the low-index surfaces of these ceramics having the NaCl structure, the (100) surface was found to be the most inert, while the (111) surface was most reactive. The (111) surfaces of these cubic ceramics are composed of alternating layers of metal and nonmetal atoms, yielding polar surfaces that are preferentially metal terminated.[31–33]

To our knowledge, only two theoretical studies have examined TiC surfaces. Fujimore *et al.*[34] used a tight binding (TB) model with parameters fit to the local density approximation (LDA) band structure results of Neckel[3] to calculate the density of states (DOS) of a five-layer (001) and a eight-layer (111) TiC film. They observed that the surface layer's valence band peak in the local DOS shifted by about 0.7 eV to higher energies as compared to that in the bulk DOS, while the surface conduction band is shifted by 0.7 eV to lower energies, thereby decreasing the band peak separation at the surface. Wimmer *et al.*[35] studied the band structure and DOS of TiC(100) using the LDA–FLAPW method for a five-layer slab. They predicted the C $2s$ and C $2p$–Ti $3d$ states to split and shift to smaller binding energies by about 0.5 eV, compared to the bulk, due to the presence of the surface. The absence of any core-level shift for the C $1s$ states demonstrated that the TiC (100) surface states are not due to a shift in the potential of the surface C atoms, but rather are due to a change in bonding at the surface, where C $2s$ and $2p$ states experience a less attractive potential compared to the bulk. Similarly, Price *et al.*[36] studied the relaxation of the TiC(100) surface using the FP-LMTO method and predicted an outward relaxation for the surface carbon atoms and inward relaxation for surface titanium atoms. Identical observations were made by Kobayashi[37] on (001) surfaces of TiC, ZrC, NbC, HfC, and TaC using LDA-based molecular dynamics calculations. To our knowledge, the present work provides the first data concerning the atomic level properties of (110) and metal-terminated (111) surfaces of TiC.

The surface energies of bcc Fe have been evaluated both experimentally[38,39] and theoretically.[40,41] The experimental surface energies have been determined from the surface tension measurements in the liquid phase extrapolated to zero temperature. First-principles calculations of the surface energies of bcc Fe have also been attempted Vitos *et al.*[40] used the full-charge-density (FCD) LMTO method under the generalized gradient approximation (GGA) to calculate the surface energies of different low index surfaces [e.g., (110), (100), (211), (310), and (111)] of ferromagnetic bcc Fe, finding the close-packed (110) to be the most stable, as expected. Similarly, Skriver and Rosengaard[41] used the Green's function LMTO method to calculate the work functions and surface energies of the bcc Fe(110) surface.

Many first-principles calculations of metal–ceramic bonding based on DFT have been reported in the last decade or so.[20,42–51] DFT, currently the most accurate method available for such studies, can reveal the atomic structure and nature of the bonding, as well as estimate adhesion energetics at these interfaces. Early theoretical work was devoted to study the interfaces involving oxide ceramics (see Ref. 20); however, other interfaces of technological importance have also been studied recently, often incorporating interfacial defects and impurities,[52,53] more diverse geometries,[54] and the effect of environment.[55]

The interfaces involving transition metal carbides and nitrides have not been explored extensively theoretically. Earlier attempts to determine the nature of interfacial bonding were confined to correlating the wetting behavior and the electronic properties of various carbides (see Ref. 56). Based on the linear dependence of the work of adhesion on the shift in energy of C $1s$ electrons, it was concluded that more stable the carbide, the smaller the wettability. Recently, Dudiy *et al.*[48,49] examined Co(001)/TiC(001) and Co(001)/TiN(001) interfaces using the plane wave pseudopotential DFT method under the GGA–PW91 (Ref. 57) approximation. They concluded that strong covalent σ bonding between Co $3d$ and C(N) $2p$ states was mainly responsible for interface adhesion. The weaker Co/TiN adhesion was explained in terms of relative energies of the N $2p$ and Co $3d$ states. Later, Dudiy found that magnetized Co at Co/TiC interfaces[50] decreases the work of adhesion, compared to nonmagnetic Co films on TiC without significantly affecting the nature of interfacial bonding. Similarly, Christensen *et al.*[51] compared Co/TiC and Co/WC interface adhesion using the plane wave pseudopotential DFT method under the

Downloaded 14 May 2003 to 128.97.45.185. Redistribution subject to AIP license or copyright, see http://ojps.aip.org/jcpo/jcpcr.jsp

GGA. The stronger adhesion observed for the Co/WC interface was attributed to substantial metallic Co–W bonding at the interface.

Fe/TiC interfaces have thus far been modeled only using less accurate theories. Mizuno *et al.*[15] studied the bonding at Fe/TiX (X=C, N, or O) interfaces using the spin-polarized discrete variational $X\alpha$ method,[25] an early version of the LDA, using a model cluster composed of two bcc Fe layers and two TiX layers (a Fe_9–Ti_9X_9 cluster) with relative orientation $(001)_{Fe}||(001)_{TiX}$ or $[110]_{Fe}||[100]_{TiX}$. They concluded that covalent bonding dominates at the interface and the strength of the Fe–Ti bond decreases going from TiC to TiN to TiO, concomitant with an increase in the Fe–X bond strength in that order. Their calculated interfacial bond strengths reflected correctly the potential for TiX to nucleate intergranular ferrite in steels. However, the lack of an extended crystal structure, with very thin layers, calls for verification of these ideas with more refined calculations. The second investigation of such interfaces employed a discrete lattice-plane (DLP) nearest-neighbor broken-bond (NNBB) approach to calculate the energetics of interfaces formed between austenite (fcc Fe) and carbides of Ti, V, Zr, and Nb.[16] The required bond energies in this approach were evaluated from the semiempirical model of de Boer *et al.*[38] They found (100)-type [fcc(100)/fcc(100)] interfaces to be the most stable, followed by (110)-type interfaces, with (111)-type fcc/fcc interfaces least stable. They concluded that lattice misfit strain in (111)-type interfaces can overwhelm chemical bonding. The approximate nature of both the $X\alpha$ cluster calculations and the semiempirical model of de Boer *et al.* also motivates the present work, where we focus our attention on the interface formed between the most stable surfaces of bcc Fe and TiC, in particular the TiC(100)/bcc Fe(110) interface, which exhibits least lattice mismatch among other possible combinations.

A good starting point leading to the evaluation of the adhesion properties of metal/ceramic interfaces is to understand the nature of bonding operative in the bulk phase and to characterize the change in the electronic structure as one goes from the bulk to the surface and finally to the interface.[42,58] Such bulk and surface calculations also provide useful calibrations of the approximations inherent in any implementation of DFT. With these goals in mind, we initiated our first-principles study of the structure and bonding of bulk bcc Fe and TiC, and then some of their low-index surfaces before coming to the Fe/TiC interface. For our investigation of coating TiC on a bcc Fe(110) substrate, we examine up to 3 ML of TiC(100). In the next section, we outline the theoretical approach used for our calculations of the bulk, surface, and interface properties. This is followed by results and analysis of the bulk and surface structural, electronic, and thermodynamic properties. Finally, predictions of the atomic structure, bonding, and adhesion at the interface are presented and implications for TiC's potential as a coating on steel are discussed.

II. CALCULATIONAL DETAILS

We performed pseudopotential plane-wave-based DFT calculations, using both the LDA and the GGA for the exchange-correlation potential, as parametrized by Perdew and Zunger[59] and Perdew *et al.*,[57] respectively. We used the "Vienna *ab initio* simulation package" (VASP),[60,61] which solves the Kohn–Sham equations using a plane wave expansion for the valence electron density and wave functions. The interactions between the ions and electrons are described by the Vanderbilt ultrasoft pseudopotentials (USPP),[62] which reduce considerably the number of plane waves required for convergence. Nonlinear partial core corrections to exchange and correlation were included for all species. We carried out spin-restricted self-consistent calculations for TiC and its surfaces and spin-polarized calculations for bcc Fe and its surfaces as well as for the TiC/bcc Fe interface. VASP uses the "traditional" self-consistency cycle to calculate the electronic ground state, where the Mermin free energy[63] is the variational quantity. Our calculations are fully converged with respect to size of the basis set [kinetic energy cutoff (E_{cutoff})] and the number of **k** points for all systems studied (Table I).

The pseudopotentials used in this study are those provided in VASP database (version 4.4). These nonlocal pseudopotentials are of the separable Kleinman–Bylander[64] form generated using the Rappe-Rabe-Kaxiras-Joannopoulos (RRKJ) scheme (see Ref. 65). The local part of the pseudopotential is the all-electron potential that has been unscreened with respect to the valence electrons beyond a given cutoff radius. The supplied database contains two sets of PP, one for LDA calculations and the other for GGA; we, of course, employed the PP appropriate for each choice of exchange-correlation potential. The atomic electronic configurations for which the respective pseudopotentials were constructed are nonmagnetic (NM) d^3s^1, s^2p^2, and d^7s^1 for Ti, C, and Fe, respectively. For titanium, we used the USPP with explicit $3p$ semicore states, whereas for carbon, we used the softer [i.e., lower default energy cutoff (E_{cutoff})] version of the pseudopotential as provided in VASP. For iron, we used the normal USPP, as provided by the VASP database, with Perdew and Wang's parametrized form of the exchange correlation under the GGA. DFT-GGA must be used for Fe, as DFT–LDA predicts the wrong ground-state bulk structure (nonmagnetic fcc Fe instead of ferromagnetic bcc Fe).[66] For Brillouin zone integration, we employed the first-order Methfessel–Paxton smearing scheme[67] using a smearing width of 0.1 eV, which resulted in a very small entropy term (<0.5 meV/atom) in all cases.

In order to study surfaces and interfaces, we used the periodic "supercell" or "slab model" approach, in which the bulk crystal is cut along the Miller plane (hkl) to expose the corresponding surface and then a number of equivalent layers of vacuum are included above this as-cut crystal surface. This extended unit cell consisting of a thin slab of crystal and vacuum is what is termed a supercell or a slab (see Fig. 1). The interface slab is created by joining the surfaces of the coating and the substrate materials. The vacuum layers then are added on the open surfaces of this interface slab. The initial interfacial separation between the coating and substrate is appropriately adjusted according to their interlayer spacings, before structural relaxation. These slabs are periodically repeated in three dimensions to obtain all transla-

Downloaded 14 May 2003 to 128.97.45.185. Redistribution subject to AIP license or copyright, see http://ojps.aip.org/jcpo/jcpcr.jsp

TABLE I. Converged parameters used for self-consistent DFT calculations on bulk TiC and bcc Fe, their surfaces, and interfaces. E_{cutoff}, $N_{\mathbf{k}}$, t_{slab}, and t_{vac} are the kinetic energy cutoffs for the plane wave basis, the number of irreducible **k** points, and the thickness of the slab and the vacuum, respectively. The numbers given in parentheses in the second column are the default E_{cutoff} for the corresponding elements, as given in the VASP database. N_{A} and N_{B} are number of atoms of types *A* and *B* contained in the bulk or the slab unit cell.

System	E_{cutoff} (eV)	$N_{\mathbf{k}}$ (Fourier grid)	t_{slab} (No. of layers) $[N_{\text{A}}, N_{\text{B}}]$	t_{vac} (Å)
TiC	278.0 (Ti–222.37) (C–211.29)	110 (10×10×10)	- [1 (Ti), 1 (C)]	-
bcc Fe	300.0 (237.51)	120 (15×15×15)	- [1 (Fe)]	-
TiC (100)	278.0	15 (10×10)	5 [5 (Ti), 5 (C)]	10
TiC (111)	278.0	30 (10×10)	7 [4 (Ti), 3 (C)]	12
TiC (110)	278.0	25 (10×10)	5 [5 (Ti), 5 (C)]	10
bcc Fe(110)	300.0	64 (15×15)	7 [7 (Fe)]	12
bcc Fe(100)	300.0	64 (15×15)	7 [7 (Fe)]	12
bcc Fe(111)	300.0	27 (15×15)	7 [7 (Fe)]	12
1 ML TiC(100)/Fe(110)	300.0	36 (6×6)	5 (Fe) + 1 (TiC) [3 (C), 3 (Ti), 25 (Fe)]	12
2 ML TiC(100)/Fe(110)	300.0	36 (6×6)	5 (Fe) + 2 (TiC) [6 (C), 6 (Ti), 25 (Fe)]	12
3 ML TiC(100)/Fe(110)	300.0	36 (6×6)	5 (Fe) + 3 (TiC) [9 (C), 9 (Ti), 25 (Fe)]	12

tional symmetry components in order to facilitate calculations in reciprocal space. The vacuum layers are added to the surface or interface to minimize interatomic interactions between periodic images of the slabs. Given that TiC and Fe surfaces are known not to undergo reconstructions,[12,38] we may employ small surface unit cells without artificial constraints due to the supercell size. Therefore, for TiC(100) and TiC(110) slabs (Fig. 1), we employed 1×1 surface geometries, where each layer contain one atom each of Ti and C, while for polar TiC(111), where each layer contains either Ti or C atoms, again a 1×1 surface geometry was employed, but the slab was terminated on both sides by a Ti layer. As mentioned earlier, these polar (111) carbide surfaces have been observed experimentally[12] to be preferentially metal terminated. For all bcc Fe surfaces, a 1×1 surface unit cell was used having one Fe atom per layer (Fig. 2).

When performing surface/interface calculations, it is important to be sure that finite-size effects inherent in the slab model do not affect the surface/interface properties. This can be achieved by ensuring that the calculations are well converged with respect to thickness of the slab (t_{slab}, for surfaces) and the vacuum region (t_{vac}, for both surfaces and interfaces). That is, we ensure that perturbations to the electronic structure due to the presence of the surface have decayed going from one side of a slab to the other. We checked the influence of varying t_{slab} and t_{vac} on the total energy per atom of the unrelaxed structures and converged our results with respect to these two parameters. The final converged values of these parameters are listed in Table I.

One other important factor is the interaction between two surfaces of the slab, because of long-range strain fields induced by ionic relaxations. The magnitude of this effect is rather dependent on surface orientation and the materials. This factor was eliminated in our calculations as we allowed relaxation for all the atoms in the slab such that the residual forces on each atom was less than 1 meV/Å.

We used the conjugate gradient method to relax the ions into their local minima. All ionic relaxations were performed by keeping unit cell shapes and volumes fixed to the equilibrium bulk structures predicted at the (appropriate) GGA or LDA level. Further, all the atoms in the slabs (both surface and interface) were allowed to relax. For surface studies, the surfaces on both sides of the slab stayed equivalent by a symmetry constraint (inversion or mirror/glide plane) located in the middle of the slab. Since our interest is to model the heteroepitaxial growth of TiC on Fe substrate, we modeled the substrate by considering a five-layer bcc Fe(110) slab, which was found to be sufficient to reliably model an infinite Fe substrate. The lattice parameters of the interface slab were determined by the bcc Fe(110) unit cell parameters which, in turn, were fixed by our GGA values for bulk bcc Fe. These interface supercells (Fig. 6, below) consisted of five layers of substrate bcc Fe(110) with 5 Fe atoms/layer and each monolayer of TiC(100) contained 3 C and 3 Ti atoms/layer. The total number of layers and atoms of each kind for all the interface supercells studied are listed in Table I. As determined from our surface calculations, we employed a vacuum thickness of 12 Å for each interface slab (Table I), which was sufficient to ensure vanishing wave function overlap across the vacuum region. The Brillouin zone integrals were per-

Downloaded 14 May 2003 to 128.97.45.185. Redistribution subject to AIP license or copyright, see http://ojps.aip.org/jcpo/jcpcr.jsp

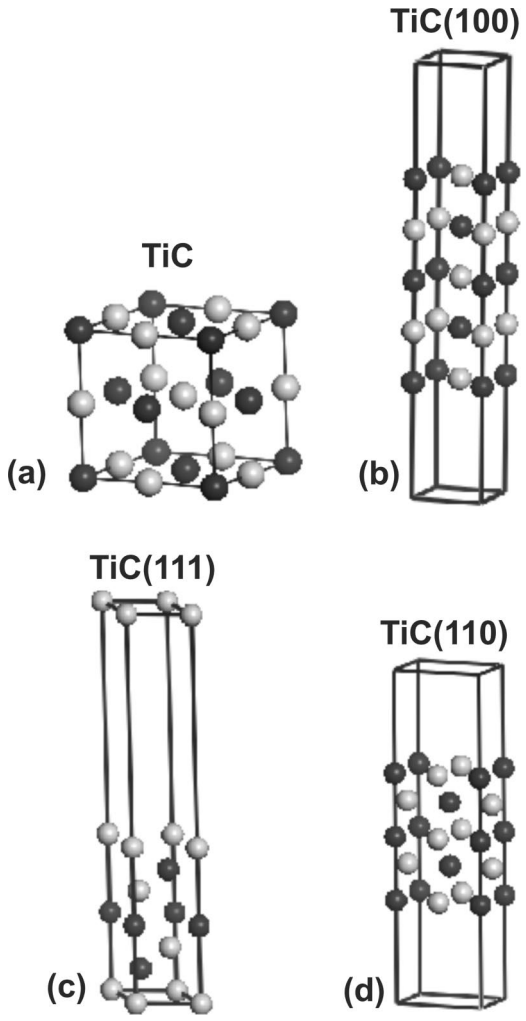

FIG. 1. (a) Bulk TiC and unrelaxed (b) TiC(100), (c) Ti-terminated TiC(111), and (d) TiC(110) surface slab unit cells used for our DFT–GGA calculations. All the surface slabs have a 1×1 surface geometry. Both TiC(100) and TiC(110) slabs are comprised of five layers with each layer containing one Ti and one C atom in the unit cell. The polar TiC(111) slab consists of seven layers having an alternating arrangement of Ti and C layers and is Ti terminated at both the ends.

formed on a $6\times6\times1$ Monkhorst–Pack grid in the reciprocal space of these interface supercells. This sampling corresponded to 18 **k** points in the irreducible wedge for relaxed (36 **k** points for unrelaxed) 1-ML-coated interface and 36 **k** points for other interfaces.

For atomic calculations, the kinetic energy cutoffs for the plane wave basis (E_{cutoff}) used were 275.0, 275.0, and 300 eV for Ti, C, and Fe atoms, respectively. These E_{cutoff} values were found to be sufficient to converge atomic energies to within 2 meV. Similarly, for bulk, surface, and interface calculations, the E_{cutoff} used are tabulated in Table I, which were found to be sufficient to converge the respective energies to within 2 meV. Calculations on isolated atoms were performed using a cubic unit cell of length 10 Å and keeping the partial occupancies fixed appropriately throughout.

The characteristic features of bonding can be best seen in the DOS and charge density plots. The DOS are projected onto atoms in different layers and decomposed inside the

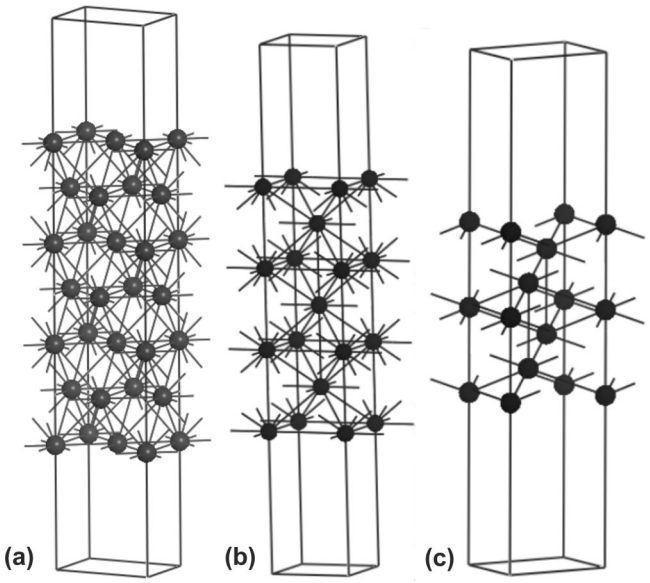

FIG. 2. Unrelaxed (a) bcc Fe(110), (b) bcc Fe(100), and (c) bcc Fe(111) surface slab unit cells used for our spin-polarized DFT–GGA calculations. Each slab has a 1×1 surface geometry and contains seven layers with one atom per layer.

atomic spheres into *l* components. The Wigner–Seitz (WS) radii used for the calculation of partial DOS *(site* and *l* projected) were 1.477 Å for Ti, 1.189 Å for C, and 1.4095 Å for Fe. These WS radii were chosen by scaling the elemental muffin-tin radii of the constituent elements to the compound in question such that a volume-filling criterion was fulfilled. Note that these spheres have nothing to do with calculations of the total energy or density, but merely determine, in a post-calculation analysis, the amount of charge density enclosed in the given sphere around each atom to derive the character of a given peak in the DOS. For our elemental Ti(hcp) and C(graphite) calculations, the WS radii (1.60 Å for Ti and 1.15 Å for C) were chosen such that the spheres captured ~95% of the total charge density, although these radii were not volume filling. This was particularly the case for C(graphite), which has an open 2D planar structure. The charge density plots include the full valence charge density; i.e., contributions from Ti $3p$ semicore and augmentation charges are also included.

III. RESULTS AND DISCUSSION

The results obtained using the above methodology are divided into two parts: those obtained for the bulk TiC and bcc Fe phases and their low-index surfaces and those obtained for the TiC(100)/bcc Fe(110) interfaces.

A. Bulk crystals and surfaces: Structural, cohesive, and electronic properties

1. Bulk properties

Again, our approach consists of going from the bulk to the surface and finally to the interface in order to analyze and understand the change in the nature of bonding and electronic structure, and also to test the accuracy of the pseudopotential approximation. The bulk structural and cohesive properties calculated include the equilibrium lattice param-

Downloaded 14 May 2003 to 128.97.45.185. Redistribution subject to AIP license or copyright, see http://ojps.aip.org/jcpo/jcpcr.jsp

TABLE II. DFT–LDA and DFT–GGA ground-state properties of bulk TiC and DFT–GGA ground-state properties of bcc Fe. For the top three entries in each cell, the top value is USPP DFT–GGA, the middle (in parentheses) is the corresponding experimental value, and the bottom value (square brackets) is USPP DFT–LDA. All-electron LDA and other USPP–GGA results are also shown. The up and down arrows for bcc Fe indicate up-spin and down-spin components.

System	Lattice parameter (Å)	Bulk modulus (B_0) (GPa)	Cohesive energy (E_{coh}) (eV/atom)	Formation energy (E_{form}) (eV/atom)	DOS at ϵ_F [$\rho(\epsilon_F)$] [(eV/atom)$^{-1}$]	Magnetic moment (μ) (μ_B)
TiC						
USPP–GGA	4.348	247	7.740	−1.921	0.127	0.00
Experiment	(4.313–4.329) [a]	(241) [b]	(7.104) [c]	(−1.906) [d]		0.00
USPP–LDA	[4.277]	[275]	[8.709]	[−1.967]	[0.108]	0.00
FPLMTO [e] (LDA)	4.329	214	8.890		0.116	
bcc Fe						
USPP–GGA	2.862	158	4.461	-	0.518 (↑) 0.285 (↓)	2.32
Experiment	(2.87) [a]	(168) [b]	(4.316) [b]	-		(2.22) [b]
KKR–LDA [f]	2.789	217	6.259	-		2.15 [d]
Other USPP–GGA [g]	2.86	155	5.150	-		2.32
Other USPP–GGA [h]	2.87	166.0	5.200			2.24

[a]Reference 68.
[b]Reference 22.
[c]Reference 1.
[d]Reference 24.
[e]Reference 32.
[f]Reference 69.
[g]Reference 70, normal valence USPP for Fe used.
[h]Reference 70, USPP that includes semicore 3*p* contributions for Fe used.

eters (a and c/a), bulk moduli (B_0), cohesive energies (E_{coh}), and energies of formation (E_{form}). In Table II, we summarize our results obtained for TiC using both the LDA and GGA. For bcc Fe, as mentioned above, we used only the spin-polarized GGA. Also given are available experimental values, all-electron FPLMTO-LDA,[32] other USPP–GGA (Moroni *et al.*[70]), and all-electron spin-polarized Korringa-Kohn-Rostaker- (KKR-) LDA (Ref. 69) results.

TiC has the NaCl (B1) structure, in which the cations and the anions independently form fcc lattices, where these two interpenetrating lattices are displaced from each other by $\mathbf{a}\langle\frac{1}{2}\frac{1}{2}\frac{1}{2}\rangle$ [see Fig. 1(a)]. The equilibrium lattice parameters for both TiC and bcc Fe were obtained by minimizing the ground-state total energy $E_T(V)$, with respect to the volume (V) (or, equivalently, the lattice parameter) of the unit cell. The E_{cutoff} values in Table I were found to be sufficient even for the smallest volume considered in the global volume minimization of E_T. As seen in Table II, the GGA slightly overestimates (by $<1\%$), whereas the LDA (consistently) slightly underestimates the lattice parameters of TiC compared with experiment.[68] The FPLMTO–LDA lattice parameter (4.329 Å) for TiC is in better agreement with experiment than our GGA results. For bcc Fe, the GGA value of equilibrium lattice parameter (2.86 Å) is in excellent agreement with experiment (2.87 Å), as well as with the USPP–GGA results of Moroni *et al.* (2.86 and 2.87 Å).

The bulk modulus (B_0) is related to the second derivative of E_T with respect to the volume, evaluated at the equilibrium volume (V_0):

$$B_0 = -V_0\left(\frac{d^2E_T}{dV^2}\right)_{V=V_0}. \tag{1}$$

Calculated values often have errors of 10% or higher. The bulk modulus was obtained by fitting the E_T–V data to the Murnaghan equation of state:[71]

$$E_T(V) = \frac{B_0V}{B_0'}\left[\frac{(V_0/V)^{B_0'}}{B_0'-1}+1\right]+C, \tag{2}$$

where B_0 is the bulk modulus, B_0' is the pressure derivative of B_0, and C is a constant. For both TiC and bcc Fe, the GGA results for B_0 are within 3–6% of the corresponding experimental values.[21,22] The LDA bulk modulus for TiC is overestimated by $\sim$10%, while the corresponding FPLMTO–LDA result is underestimated by the same amount, indicating inaccuracies in the LDA USPPs.

The cohesive energies (E_{coh}) in Table II were calculated in the usual way from the difference in total energies between isolated atoms and the A_xB_y compound:

$$E_{coh}(A_xB_y) = [xE_T^{at}(A) + yE_T^{at}(B)] - E_T(A_xB_y). \tag{3}$$

Cohesive energies output by VASP are with respect to the nonmagnetic reference configurations used to generate the pseudopotentials, even though, e.g., the true ground state of Ti is high spin s^2d^2 (^{3}F), not NM s^1d^3. Therefore, we require the energy difference ($\Delta E_{at} = E_{at}^{NM} - E_{at}^{g.s.}$) in order to correct VASP cohesive energies and report E_{coh} referenced to the experimental ground states of the atoms. Our GGA (LDA) calculated value of ΔE_{at} for Ti was 2.289 (2.228) eV which is consistent with the 2.24 (1.99) eV value reported in the VASP manual. Similarly, for Fe the true ground state is high spin s^2d^6 (^{5}D), though the pseudopotential was constructed using a NM d^7s^1 configuration, and for C, the true ground state is high spin s^2p^2 (^{3}P), not NM s^2p^2. Our DFT–GGA values of ΔE_{at} for Fe and C atoms are 3.848 and 0.950 eV, respectively. The corresponding LDA value for C

Downloaded 14 May 2003 to 128.97.45.185. Redistribution subject to AIP license or copyright, see http://ojps.aip.org/jcpo/jcpcr.jsp

atom is 0.910 eV. Taking these energy differences into account yields cohesive energies of TiC [GGA (LDA)] and Fe [GGA] of 7.740 (8.709) and 4.461 eV/atom, respectively. Overall, the GGA results for both TiC and Fe are in much better agreement with experiment [$E_{\mathrm{coh}}^{\mathrm{expt}}(\mathrm{TiC}) = 7.104$ eV/atom and $E_{\mathrm{coh}}^{\mathrm{expt}}(\mathrm{Fe}) = 4.316$ eV/atom] than the LDA results, though still off by $\sim 10\%$. The remaining error is due to systematic errors in the description of exchange-correlation, e.g., the spurious self-interaction terms.[72] USPP–GGA (Moroni *et al.*) cohesive energies for bcc Fe deviate from experiment by as much as 15%; this is due in part to improperly accounting for the final states of the atoms.

The systematic errors in E_{coh} can be minimized by instead considering the energy of formation (E_{form}), where isolated atomic contributions will cancel out:

$$E_{\mathrm{form}}(A_xB_y) = E_{\mathrm{coh}}(A_xB_y) - xE_{\mathrm{coh}}^{\mathrm{g.s.}}(A) - yE_{\mathrm{coh}}^{\mathrm{g.s.}}(B). \quad (4)$$

This is reflected in the E_{form} value for TiC, which agrees quite well (within 1%) with the experimental value.[24] Our DFT–GGA cohesive energies for Ti(hcp) and C(graphite), properly referenced to the true atomic ground states, are 5.463 and 8.097 eV/atom, respectively. The corresponding LDA values are 6.285 and 9.165 eV/atom, respectively.

The metallic character of TiC and Fe is evident from the nonzero DOS at the Fermi level $\rho(\epsilon_F)$ (Table II) and the ferromagnetic nature of bcc Fe produces $\mu = 2.315\mu_B$, in good agreement with the experimental value of $2.22\mu_B$ and USPP-GGA values (Moroni *et al.*) of $2.32\mu_B$ and $2.24\mu_B$ (Table II). These features are evident also in total DOS and *site* and *l* projected for TiC (Fig. 3) and bcc Fe (Fig. 5, below). For example, the spin-polarized DOS for bcc Fe [Fig. 5(a)] is clearly dominated by Fe *d* states with negligibly small contributions coming from Fe *s*, which is mostly delocalized.

The DOS of bulk TiC provides evidence for both metallic (finite DOS at ϵ_F) and covalent Ti–C bonding [Fig. 3(a)]. A low-lying band at ~ -9.5 eV exhibits almost exclusively C $2s$ character, while at higher energies, one observes three overlapping bands (~ -4.0 eV, ~ -3.0 eV, and ~ -2.0 eV) separated from the C $2s$ band by an energy gap. These overlapping bands consist of not only the C $2p$ states but also Ti *d* states, indicating a strong interaction between C $2p$ and Ti $3d$ electrons. This band represents the main covalent bonding component, exhibiting strong mixing. The corresponding antibonding band lies in the unoccupied region ($\sim +4.0$ eV). These results are consistent with previous LDA predictions[3,8,11] on carbides of Ti, V, Zr, and Nb.

An ionic component of the bonding also exists, in which electron transfer from Ti to C occurs (see Table III). This has been observed by other workers,[3,8] independent of the radii of the Wigner–Seitz spheres selected. Our choice of Wigner–Seitz radii suggests that Ti loses $\sim 0.1e$ and C gains $\sim 0.4e$, compared to the respective bulk elements (see Table III). This loss–gain inequivalency here is indicative of the limitations of this type of analysis (arbitrary choice of sphere radii); therefore only qualitative conclusions should be drawn. A comparison of the *l*-decomposed charges between bulk TiC and respective bulk elements qualitatively suggests

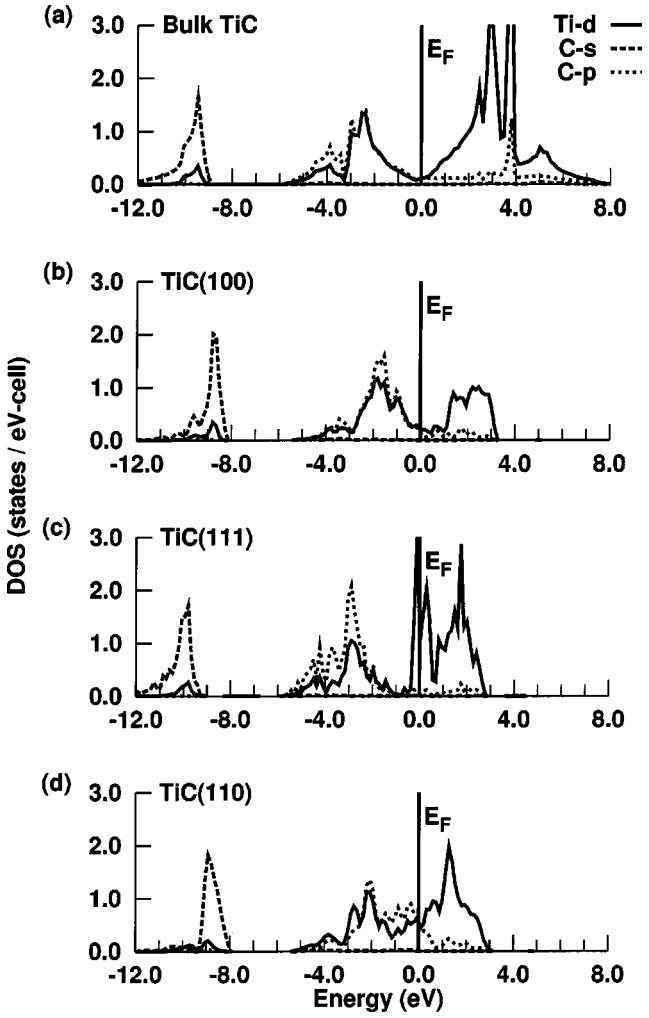

FIG. 3. The *site*- and *l*-projected partial density of states (DOS) for (a) bulk TiC and the surface layer of (b) TiC(100), (c) polar Ti-terminated TiC(111) (surface Ti and subsurface C), and (d) TiC(110).

that Ti *s* electrons are donated to C *p* states. This is exactly what is expected based on ionization energies (IEs): IE(Ti s) $<$ IE(Ti d). Charge transfer here for TiC is somewhat lower than that obtained by the APW–LDA calculations of Neckel,[3] which predicted a loss of $0.36e$ by Ti and a gain of $0.43e$ by C. The all-electron LDA calculations of Wimmer *et al.*[35] predicted the charge transfer to be $0.29e$ from Ti to C. However, the qualitative feature of electron transfer from Ti to C is found by all three sets of calculations.

The total valence electron density distribution in the (100) plane [Fig. 4(a)] of TiC is also suggestive of this charge transfer from Ti to C, given the nearly spherically symmetric charge density around each C atom, indicative of a close to half-filled *p* shell. Some localized Ti–C interactions are also evident in the (100) plane of TiC.

2. Surface properties

Here we discuss predictions of structural and electronic properties for the (100), (110), and (111) surfaces of both

Downloaded 14 May 2003 to 128.97.45.185. Redistribution subject to AIP license or copyright, see http://ojps.aip.org/jcpo/jcpcr.jsp

TABLE III. Partial electronic charges (Q_l) of C, Ti, TiC, and Fe, partitioned according to their angular momentum, for bulk and surface (S) atoms inside their Wigner–Seitz spheres. Q_T's are the total number of valence electrons inside the Wigner–Seitz sphere. The up and down arrows for bcc Fe surfaces indicate up-spin and down-spin components, respectively, and μ is the magnetic moment (in μ_B/atom) for Fe atoms in bulk or surface layers.

	C				M = Ti/Fe [a]				
System	Q_s	Q_p	Q_d	Q_T	Q_s	Q_p	Q_d	Q_T	μ (μ_B/atom)
C(gr) [b]	1.420	2.142	0.270	3.832					-
Ti(hcp) [b]					0.532	6.465	2.374	9.371	-
TiC	1.431	2.698	0.077	4.204	0.348	6.542	2.364	9.254	-
TiC(100)									-
(S)	1.430	2.551	0.058	4.039	0.337	6.468	2.304	9.109	
TiC(111) (S)	-	-	-	-	0.368	6.392	2.341	9.101	-
(S-1)[c]	1.436	2.752	0.098	4.287	-	-	-	-	
TiC(110)									-
(S)	1.447	2.403	0.049	3.899	0.346	6.404	2.366	9.115	
bcc Fe									2.320
(↑)					0.255	0.263	4.399	4.917	
(↓)					0.270	0.329	1.985	2.584	
Fe(110)									2.742
(S)(↑)					0.258	0.212	4.545	5.015	
(S)(↓)					0.260	0.227	1.786	2.273	
Fe(100)									3.046
(S)(↑)					0.258	0.192	4.640	5.091	
(S)(↓)					0.248	0.195	1.601	2.045	
Fe(111)									2.978
(S)(↑)					0.262	0.171	4.624	5.057	
(S)(↓)					0.248	0.161	1.670	2.079	

[a]The Ti values reflect integration of charges including the $3p$ semicore electrons.
[b]The Wigner–Seitz sphere radii selected for evaluation of partial charges for Ti (hcp) and C (gr) phases are 1.60 and 1.15 Å, respectively.
[c]There are no surface C atoms for the metal-terminated TiC(111) surface.

TiC and bcc Fe. The properties evaluated are the surface energies, relaxations, and electronic properties, e.g., DOS, surface states, and charge transfer effects.

The surface energy E_{surf} is approximated in the slab model as

$$E_{\text{surf}} = \frac{\left[E_{\text{slab}} - \left(\frac{N_{\text{slab}}}{N_{\text{bulk}}}\right) E_{\text{bulk}}\right]}{2A}, \tag{5}$$

where E_{slab} and E_{bulk} are the total energies of the surface slab and the bulk unit cell, respectively, where we are neglecting finite temperature contributions to the surface free energy. N_{slab} and N_{bulk} are the number of formula units contained in the slab and the bulk supercells, respectively. A is the area of the surface unit cell.

a. TiC surfaces. All the low-index surfaces of TiC are observed to undergo minimal structural relaxations, as can be

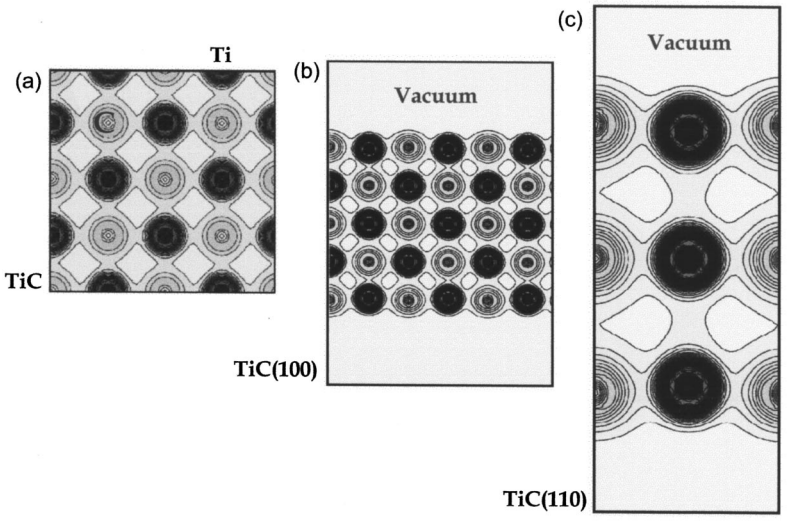

FIG. 4. Total valence charge density distributions, each sliced through both Ti and C atoms, on the (a) (001) plane of bulk TiC, depicting c p–Ti d interactions, (b) (011) plane of TiC(100), and (c) (001) plane of TiC(110), depicting p–d and d–d interactions. Both the surface slices show corrugation of charges over C atom. The charge concentration is proportional to the depicted intensity. Note that the Ti density includes the $3p$ semicore electrons.

Downloaded 14 May 2003 to 128.97.45.185. Redistribution subject to AIP license or copyright, see http://ojps.aip.org/jcpo/jcpcr.jsp

TABLE IV. Vertical displacements [Δz, (Å)] perpendicular to the surface, upon relaxation of the surface (S) and directly subsurface (S-1) atoms, from bulk-terminated positions. Minus signs indicate movement into the bulk. d_i is interlayer distance between the layer in question and the next layer below. The values in parentheses are for the unrelaxed slabs.

	(**C**)		(*M* = **Ti/Fe**)	
System	Δz (Å)	d_i (Å)	Δz (Å)	d_i (Å)
TiC(100)				
(S)	0.030	2.204 (2.192)	−0.077	2.113 (2.174)
(S-1)	0.012	2.186 (2.174)	−0.016	2.159 (2.174)
TiC(111)				
(S)	-	-	−0.156	1.025 (1.256)
(S-1)	−0.007	1.407 (1.255)	-	-
TiC(110)				
(S)	0.007	1.496 (1.537)	−0.137	1.379 (1.537)
(S-1)	0.047	1.585 (1.537)	+0.022	1.559 (1.537)
Fe(110)				
(S)			−0.002	2.017 (2.024)
(S-1)			0.005	2.033 (2.024)
Fe(100)				
(S)			−0.020	1.374 (1.431)
(S-1)			0.037	1.465 (1.431)
Fe(111)				
(S)			−0.086	0.797 (0.826)
(S-1)			−0.057	0.648 (0.826)

seen in Table IV. The maximum relaxation is observed in polar TiC(111), where the surface Ti atoms move into the bulk by about 0.156 Å, thereby reducing the interlayer separation between the surface and subsurface layers. Overall, the (100), (110), and (111) surfaces of TiC show nearly ideal bulk truncation consistent with 1×1 patterns as also observed by LEED experiments.[12] The possibility of a rippled relaxation, i.e., C and Ti rows displaced in opposite directions on the TiC(100) surface, was considered in impact collision ion scattering spectroscopy[73] (ICISS) experiments, but the measurements indicated an ideal bulk truncation, although a very small rippled relaxation could not be ruled out. FPLMTO (Ref. 32) predictions of a rippled relaxation on the TiC(100) surface showed surface C atoms moving slightly toward vacuum (+0.02 Å) and Ti atoms moving slightly into the bulk (−0.04 Å). From Table IV, we find the magnitude of this rippling to be +0.030 Å for carbon and −0.077 Å for Ti, in qualitative agreement with FPLMTO results. The FPLAPW calculations[35] also predicted rippling, but with opposite directions of Ti and C displacements. The effect is small enough that one should consider this to be in the noise of the calculational method: the surface is essentially bulk terminated.

The electronic structure of TiC(100) reveals several surface-induced features [see Fig. 3(b)]. A comparison with the bulk DOS [Fig. 3(a)] shows that new states appear in the energy range between −4.0 eV and +4.0 eV around the Fermi level. The C $2p$ and Ti $3d$ peaks in the occupied part of DOS shift towards lower binding energy by about 0.5 eV, thereby reducing the valence band width and enhancing the degree of localization of electrons at the surface. Similar DOS shifts were predicted by FPLAPW (Ref. 35) and TB (Ref. 34) calculations for TiC(100).

TABLE V. DFT–GGA surface energies [E_{surf} (mJ/m^2)] of low-index surfaces (both unrelaxed and relaxed) of TiC and bcc Fe. Values in parentheses are DFT–LDA results for the most stable surface of TiC. The change in energy upon relaxation [ΔE_{relax} (meV/formula unit)].

System	E_{surf} (unrelaxed) (mJ/m^2)	E_{surf} (relaxed) (mJ/m^2)	ΔE_{relax} (meV/formula unit)
TiC (100)	1799 (2492)	1665 (2254)	31.7 (56.0)
TiC (111)	3613	3122	77.3
TiC (110)	3891	3631	86.7
bcc Fe(110)	2289	2288 [2417-2475] [a] {2430} [b]	0.1
bcc Fe(100)	2323	2301	3.2
bcc Fe(111)	2667	2586 [2733] [b]	20.3

[a]Experimental (Refs. 38 and 39).
[b]FCD–LMTO (GGA) (Ref. 40).

The partial DOS for TiC(111) projected onto surface Ti and subsurface C atoms [Fig. 3(c)] shows a dip at around −1.0 eV in the occupied part of the valence band, which separates the covalent Ti d–C p mixing region at higher binding energy and the totally Ti d-dominated region at the Fermi level that reveals the metallic character of the surface layer. By contrast, partial DOS for TiC(110) exhibits primarily Ti d–C p covalent interactions [Fig. 3(d)]. The partial charges for surface Ti and C atoms (Table III) suggest only small changes compared to bulk TiC, with the general trend of some charge transfer from Ti to C remaining upon formation of surfaces.

Our fully converged DFT–GGA results for the surface energies of various unrelaxed and relaxed surfaces of TiC and bcc Fe are given in Table V. For comparison, we also show LDA results for the most stable surface of TiC, viz., TiC(100). As usual, the LDA surface energy is much higher than the GGA one. Generally, the higher the packing density of a given surface, the more stable the surface. The theoretical packing densities of (100), (110), and (111) surfaces of NaCl-like structures (here TiC) are roughly in the ratio $1.000:0.530:0.577$ $[4/a^2:3/(a^2\sqrt{2}):4/(a^2\sqrt{3})]$, suggesting a stability sequence of (100)>(111)>(110). Our calculated stabilities of low-index surfaces of TiC indeed follow packing densities, as can be seen from the surface energy values for the relaxed structures in Table V. Note that we found the polar TiC(111) surface to be preferentially Ti terminated [other (111) surface terminations yielded much higher surface energies], as also observed experimentally.[12]

The surface energy values can serve as a guideline for predicting the critical stress required for crack propagation in a brittle material, which, according to Griffith theory,[74] is proportional to twice the surface energy. For ductile materials (e.g., Fe metal), where the plastic deformation energy plays a more conclusive role, the proportionality to the surface energy is still valid, as a first approximation.[74] Our DFT–GGA surface energy values (Table V) indicate that the critical stress required for crack propagation in bcc Fe along [110] is about 27% larger than that in TiC along [100].

b. bcc Fe surfaces. Like TiC, the low-index surfaces of

Downloaded 14 May 2003 to 128.97.45.185. Redistribution subject to AIP license or copyright, see http://ojps.aip.org/jcpo/jcpcr.jsp

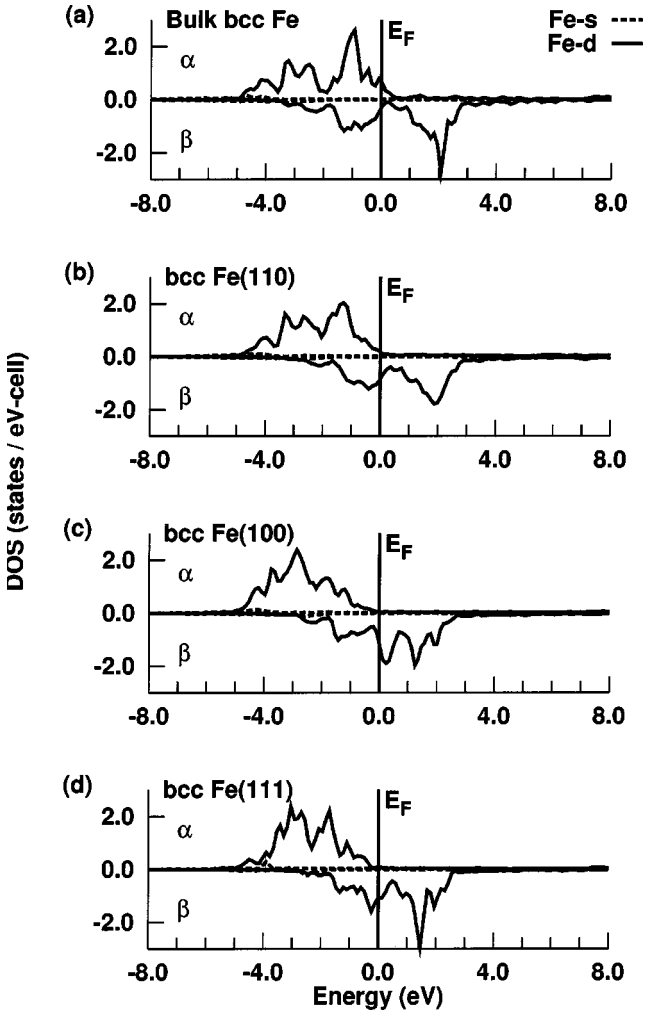

FIG. 5. Spin-polarized *site*- and *l*-projected partial DOS for (a) bulk bcc Fe and the surface layer of (b) Fe(110), (c) Fe(100), and (d) Fe(111). The α and β correspond to up-spin and down-spin partial DOS.

bcc Fe also exhibit nearly negligible structural relaxation (see Table IV). The Fe(110) shows almost perfectly smooth termination. For bcc Fe(100), the surface atoms move into the bulk, while the subsurface atoms move out toward vacuum, thereby decreasing the interlayer separation by about 0.057 Å. In Fe(111), both surface and subsurface atoms move into the bulk by 0.086 Å and 0.057 Å, respectively, and the interlayer separation decreases by 0.029 Å.

The partial DOS plots (Fig. 5) for surface Fe atoms show that the (110) surface looks quite bulk like [compare Figs. 5(a) and 5(b)], while the (100) and (111) surfaces show larger shifts in the occupied states that differ for up and down spin channels. This leads to net magnetic moments for the surface Fe atoms in Fe(110), Fe(100), and Fe(111) of $2.742\mu_B$/atom, $3.046\mu_B$/atom, and $2.978\mu_B$/atom (see Table III) as compared to $2.32\mu_B$/atom for bulk Fe. The integrated valence electron charges (up spin + down spin) for Fe atoms in the bulk and at the (110), (100), and (111) surfaces are 7.4*e*, 7.3*e*, 7.1*e*, and 7.1*e*, respectively. The decrease in integrated charges at the surfaces is no doubt due to delocalization of the electron density tails into the vacuum. Despite this, we see that the close-packed (110) surface has very nearly a bulk electronic structure (based on the integrated charges), but with an enhanced magnetic moment. Indeed all three surfaces exhibit increased magnetism at the surface. The bulklike electronic structure of the (110) surface is partially responsible for its greater stability.

The stability trend of bcc Fe surfaces (see Table V) also follow their packing density sequence, viz., (110)>(100)>(111). Experimental surface energies (extrapolated to 0 K) of bcc Fe(110) vary between 2417 and 2475 mJ/m^2.[38,39] The GGA slightly underestimates the surface energy, yielding a value of 2288 mJ/m^2.

To summarize, the stability of all the low-index surfaces of both TiC and bcc Fe follow their packing density sequence. All the surfaces show negligible relaxations with almost ideal bulk termination. While the (100) and (110) surfaces of TiC are predominantly polar covalent in nature, the metal-terminated TiC(111) surface shows strong metallicity at the surface in addition to the polar covalent component. All surfaces of Fe are predicted to exhibit enhanced magnetism.

B. TiC(100)/Fe(110) interface

Here we focus on the structure, bonding, and energetics at the TiC/Fe interface. We have restricted our study to the interface formed between the most stable surfaces, viz., TiC(100) and bcc Fe(110), as it is observed experimentally[17] that stable interfaces are generally formed between most stable surfaces. Although more open surfaces might bond more strongly to each other because of the higher number of dangling bonds, these more open surfaces also have higher surface tensions,[17] and therefore, the deciding factor is the relative bond strength at the interface in relation to that in the bulk. The other reason for selecting this particular interface is that it has a minimum lattice mismatch (2.1%) among all combinations considered of low-index surfaces of TiC and bcc Fe, suggesting it will be the least strained and therefore the most likely to be the most stable interface. In order to achieve asymptotic values for the properties of the coating, we progressively increased the thickness of the TiC coating from one monolayer to three monolayers.

1. Interface structure

The geometrical aspect of matching TiC to the bcc Fe substrate is relatively simple to approach: some surface unit cell of TiC(100) with surface area A_2 is forced into registry with a bcc Fe(110) surface unit cell with surface area A_1 and an overlap area Ω is then calculated. The misfit parameter ζ defined as[17]

$$\zeta = \frac{2\Omega}{A_1 + A_2}, \tag{6}$$

is then calculated to select lattice vectors for the surface slabs which correspond to minimum ζ. One needs to be careful in this analysis, as excellent matching can be produced by considering some exotic Miller indices for very large interface unit cells. An analysis of surface matching provided us with a practical interface unit cell having a supercell area of 28.97 Å^2 ($a=9.386$ Å and $b=4.048$ Å) and a lattice mismatch of 2.1%.

Downloaded 14 May 2003 to 128.97.45.185. Redistribution subject to AIP license or copyright, see http://ojps.aip.org/jcpo/jcpcr.jsp

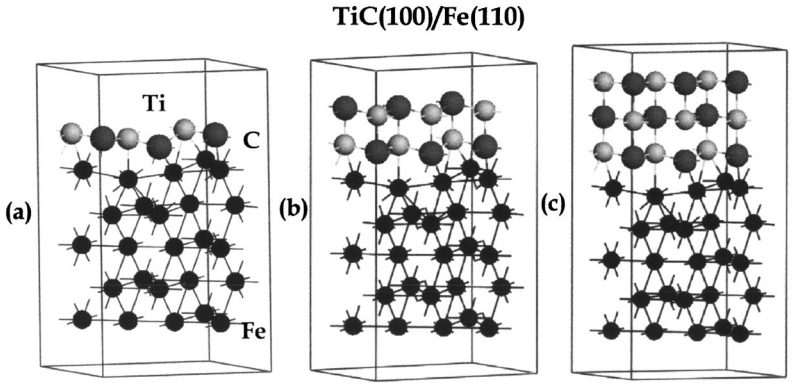

FIG. 6. Structurally relaxed TiC(100)/Fe(110) interface slab unit cells for (a) 1-ML-, (b) 2-ML-, and (c) 3-ML-thick coatings of TiC. The Fe substrate has five layers with five atoms per layer. Each ML of TiC contains three atoms each of Ti and C.

The main structural features of the relaxed TiC/Fe interfaces (Fig. 6) are listed in Table VI, which gives coordination numbers and nearest-neighbor distances for atoms at or near the relaxed interface. The atoms have been designated according to their distances from the interface, e.g., atom C_1 is closer to the interface region than atom C_2 and so forth. For a 1-ML TiC coating [Fig. 6(a)], the calculated Fe–C distances are 2.05 and 2.07 Å for C_1 and C_2, respectively (see Table VI). The experimental value of the Fe–C distance in Fe_3C is 2.02 Å,[68] which is close to the interface Fe–C values, suggesting strong Fe–C bonding at the interface. The minimum Fe–Ti bond lengths in the relaxed interface are 2.29 and 2.45 Å for Ti_1 and Ti_2, respectively. These are

TABLE VI. Rough number of nearest neighbors (#nn) and their distance ranges [d_{nn} (Å), in parentheses] for atoms positioned at (subscript 1) and near (subscripts 2 and 3) the TiC/Fe interface. Bulk and surface atom coordination analyses for isolated TiC and Fe are also included for comparison. The subscripts *s* and *b* refer to surface and bulk atoms, respectively.

		#nn [d_{nn} (Å)]		
System	Atom	C	Ti	Fe
TiC	C	-	6 (2.17)	
	Ti	6 (2.17)	-	
TiC(100)	C_s		5 (2.18–2.22)	
	C_b		6 (2.16–2.17)	
	Ti_s	5 (2.08–2.18)		
	Ti_b	6 (2.17–2.19)		
bcc Fe(110)	Fe_s			2 (2.47) + 2 (2.86)
	Fe_b			4 (2.48) + 4 (2.86)
1 ML	C_1		4 (2.14–2.22)	1 (2.05)
TiC(100)/Fe(110)	C_2		4 (2.18–2.27)	2 (2.07)
	Ti_1	4 (2.18–2.22)		1 (2.29)
	Ti_2	4 (2.14–2.27)		1 (2.45) + 1 (2.70)
	Fe_1	1 (2.05)	1 (2.70)	2 (2.54) + 6 (2.61–2.79)
	Fe_2	1 (2.07)	1 (2.45)	7 (2.43–2.55) + 1 (2.79)
2 ML	C_1		4 (2.10–2.20)	1 (1.99)
TiC(100)/Fe(110)	C_2		5 (2.18–2.25)	2 (2.26–2.29)
	C_3		5 (2.12–2.22)	
	Ti_1	5 (2.12–2.22)		1 (2.49) +1 (2.74)
	Ti_2	5 (2.18–2.20)		1 (2.51)
	Ti_3	5 (2.10–2.22)		
	Fe_1	1 (1.99)	1 (2.74)	7 (2.55–2.67)
	Fe_2	1 (2.26)	1 (2.48)	7 (2.38–2.55)
	Fe_3		1 (2.51)	2 (2.26–2.28) + 6 (2.51–2.58)
3 ML	C_1		5 (2.13–2.20)	1 (1.99)
TiC(100)/Fe(110)	C_2		5 (2.19–2.45)	2 (2.24–2.27)
	C_3		6 (2.09–2.20)	
	Ti_1	5 (2.09–2.23)		1 (2.52) + 1 (2.76)
	Ti_2	5 (2.17–2.20)		1 (2.57)
	Ti_3	6 (2.16–2.22)		
	Fe_1	1 (1.99)	1 (2.76)	7 (2.55–2.69)
	Fe_2	1 (2.27)	1 (2.51)	7 (2.38–2.55)
	Fe_3		1 (2.57)	8 (2.27–2.58)

Downloaded 14 May 2003 to 128.97.45.185. Redistribution subject to AIP license or copyright, see http://ojps.aip.org/jcpo/jcpcr.jsp

shorter than the experimental Fe–Ti bond length in bulk FeTi ($Pm\bar{3}m$) (2.58 Å),[68] indicating also strong Fe–Ti bonding at the TiC/Fe interface. In both relaxed 2-ML and 3-ML coatings [Figs. 6(b) and 6(c)], the Fe_1–C_1 distance is reduced slightly to 1.99 Å, compared to 1-ML coating, indicating slightly increased Fe–C interactions. By contrast, the minimum Fe–Ti bond distances are 2.49 and 2.52 Å, respectively, for 2-ML and 3-ML coatings, indicating decreased Fe–Ti interactions as compared to the 1-ML film, but comparable interactions to those in bulk FeTi. The minimum Fe–C_2 bond distances are 2.07, 2.26, and 2.24 Å, respectively, for 1-, 2-, and 3-ML films, while the minimum Fe–Ti_2 bond distances are 2.45, 2.51, and 2.57 Å, respectively. This indicates progressively decreasing Fe–Ti interactions as coating thickness increases. The Fe–C_2 interaction reduces going from 1-ML to 2-ML coating, but then it increases slightly going from the 2-ML to 3-ML case. The Fe_3 atoms, in the layer adjacent to the interface layer, exhibit interactions with Ti atoms (Table VI), indicating high coordination of these metal atoms. A comparison of various interatomic distances for the relaxed interface supercells and those in the bulk phases (Table VI) shows that these interfaces are more or less smooth with very little relaxations (Fig. 6).

2. Interfacial bonding

The characteristic features of bonding across the 1-ML film's interface can be seen in partial DOS plots in Fig. 7, where we display spin-polarized *site*- and *l*-projected DOS for the constituent atoms. Figure 7(a) shows a strong interaction between C_1 $2p$ and Fe_1 d electrons in the valence band, which is the main covalent component of bonding across the interface. Similarly, mixing of Ti_1 d–Fe_1 d states can also be observed in this plot, although most of Ti d band is unoccupied. The partial DOS for the interface atoms also show a finite DOS at the Fermi level, indicating metallic bonding across the interface, arising mainly because of Ti_1 d and Fe_1 d states. Taking into account the higher coordination of Ti and Fe than C, it may be concluded that both Fe–Ti and Fe–C interactions contribute strongly to the interfacial bonding. In Fig. 7(a), the strong peak contributing to Fe–C bonding in the lower part of valence band is depleted in DOS of C_2 and Fe_2 [Fig. 7(b)], indicating reduced covalent bonding with increased bond distance. A comparison of total valence charges of these interfacial atoms (Table VII) with their corresponding surface values (Table III) shows that C_1 and Fe_1 gain $\sim 0.02e$ and $\sim 0.11e$, respectively, while Ti_1 loses about $0.07e$, as compared to their surface values, although all charges are well below their respective bulk values. Similarly, C_2 and Fe_2 gain $\sim 0.05e$ and $\sim 0.33e$, respectively, while Ti_2 loses $\sim 0.11e$. Thus, the Fe–TiC interface bonding involves a small amount of electron transfer from Ti to Fe. Further, the *l*-decomposed spin-polarized charges in Table VII also show that Fe substrate induces magnetization in the neighboring TiC layer, which affects Ti d states much more than C p states (Ti_2 more than Ti_1), indicating that these d states are definitely involved in the interfacial bonding. Moreover, the interface Fe atoms have much reduced magnetic moments ($Fe_1 = 2.392\mu_B$ and $Fe_2 = 1.941\mu_B$) compared to their surface value of $2.742\mu_B$, suggesting strong spin pairing is involved in Fe–Ti interactions.

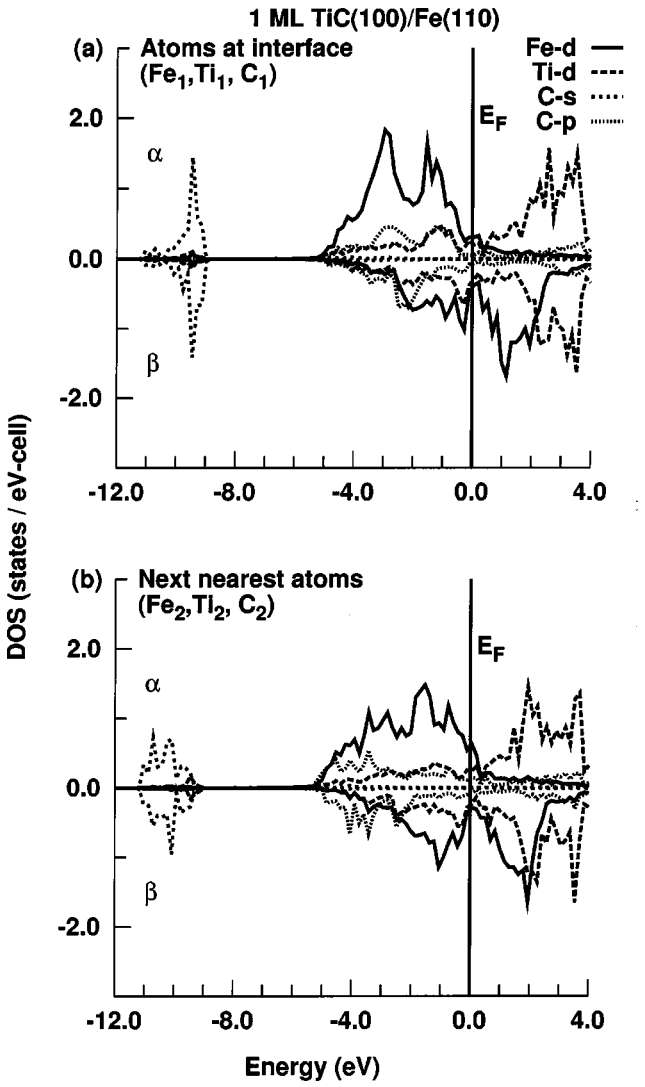

FIG. 7. Spin-polarized *site*- and *l*-projected partial DOS for atoms (a) nearest, and (b) next nearest to the interface for 1 ML of TiC on a bcc Fe(110) substrate. These atoms are designated with subscripts 1 and 2, respectively (see also Table VI). The α and β correspond to up-spin and down-spin partial DOS.

The bonding features in 2- and 3-ML-thick coatings are identical in many respects. Hence, for the sake of brevity, we restrict our discussion to only the 2-ML case, pointing out differences, if any, in the 3-ML coating. The spin-polarized partial DOS for a 2-ML coating [Fig. 8(a)] shows that the Ti_1 d DOS in the occupied part of the valence band has diminished with a concomitant increase in the C_1 p contribution in the lower part of the valence band compared to the 1-ML case (Fig. 7). The DOS at the Fermi level is clearly dominated by Fe d states with almost negligible participation from Ti_1 d states, suggesting much reduced intermetallic bonding at the interface. The progressive increase in Ti d–C p covalent mixing can be observed going from first nearest neighbors to third nearest neighbors [Figs. 8(a), 8(b), and 8(c)], indicating progressive increase in intraceramic bonding as one moves away from the interface. The Ti_3 d states still contribute to Fe–Ti bonding at the second-nearest-neighbor

Downloaded 14 May 2003 to 128.97.45.185. Redistribution subject to AIP license or copyright, see http://ojps.aip.org/jcpo/jcpcr.jsp

TABLE VII. Spin-polarized partial electronic charges (Q_l), partitioned according to its angular momentum inside its Wigner–Seitz sphere, for atoms nearest (subscript 1) and next nearest (subscript 2) to the TiC(100)/Fe(110) interface. Q_T's are the total number of valence electrons inside the Wigner–Seitz sphere. Atom-resolved magnetic moments μ_a (μ_B) are also given.

		1 ML		2 ML		3 ML	
System		(↑)	(↓)	(↑)	(↓)	(↑)	(↓)
C_1	Q_s	0.713	0.712	0.714	0.715	0.715	0.715
	Q_p	1.291	1.273	1.368	1.368	1.346	1.350
	Q_d	0.036	0.036	0.051	0.051	0.052	0.049
	Q_T	2.041	2.021	2.134	2.134	2.112	2.114
	μ_a	0.020		0.000		−0.002	
C_2	Q_s	0.708	0.708	0.703	0.700	0.703	0.700
	Q_p	1.280	1.295	1.318	1.314	1.297	1.284
	Q_d	0.046	0.046	0.042	0.041	0.041	0.039
	Q_T	2.035	2.049	2.063	2.055	2.041	2.023
	μ_a	−0.014		0.008		0.018	
Ti_1	Q_s	0.166	0.164	0.181	0.185	0.179	0.183
	Q_p	3.209	3.205	3.267	3.273	3.264	3.272
	Q_d	1.058	1.237	1.155	1.247	1.167	1.236
	Q_T	4.434	4.607	4.603	4.705	4.610	4.691
	μ_a	−0.173		−0.102		−0.081	
Ti_2	Q_s	0.160	0.170	0.168	0.168	0.168	0.165
	Q_p	3.206	3.207	3.243	3.238	3.240	3.234
	Q_d	1.011	1.249	1.118	1.214	1.140	1.175
	Q_T	4.377	4.626	4.529	4.620	4.548	4.574
	μ_a	−0.249		−0.091		−0.026	
Fe_1	Q_s	0.247	0.246	0.244	0.247	0.243	0.246
	Q_p	0.270	0.313	0.275	0.316	0.273	0.310
	Q_d	4.377	2.503	4.389	1.950	4.407	1.929
	Q_T	4.895	2.503	4.908	2.513	4.923	2.485
	μ_a	2.392		2.395		2.438	
Fe_2	Q_s	0.260	0.269	0.252	0.265	0.252	0.264
	Q_p	0.293	0.346	0.267	0.308	0.267	0.306
	Q_d	4.224	2.221	4.399	2.016	4.420	1.989
	Q_T	4.777	2.836	4.917	2.588	4.938	2.559
	μ_a	1.941		2.329		2.379	

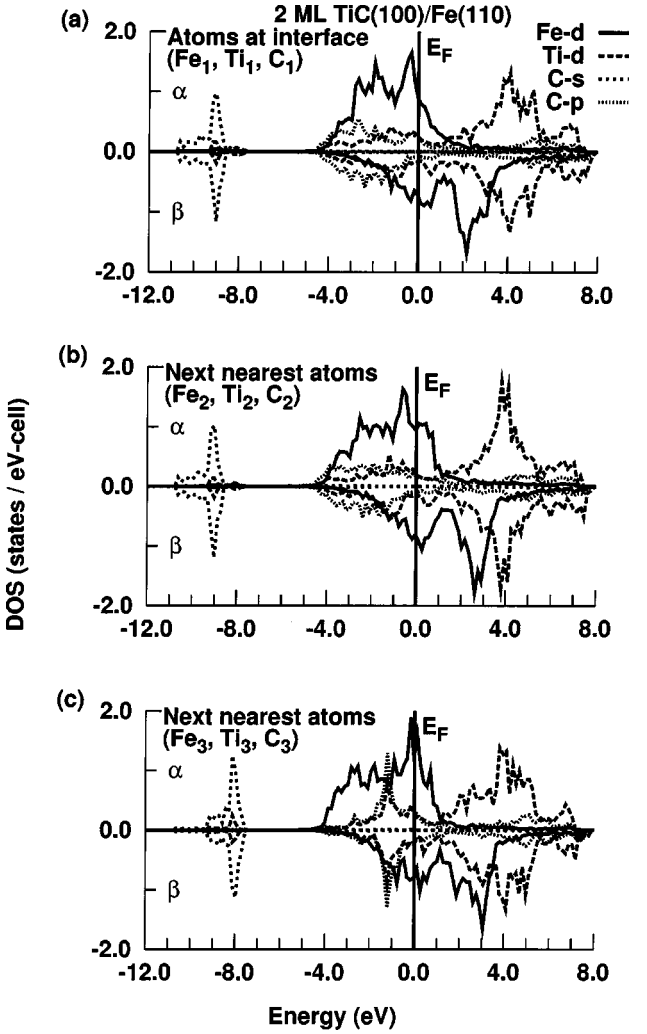

FIG. 8. Spin-polarized *site*- and *l*-projected partial DOS for atoms (a) nearest (b) second nearest, and (c) third nearest to the interface for 2 ML of TiC on the Fe(110) substrate. These atoms are designated with subscripts 1, 2, and 3, respectively (see also Table VI). The α and β correspond to up-spin and down-spin partial DOS.

level [see Fig. 8(c)]. This shows that for a 2-ML coating, although there is a slight increase in Fe–C interactions, the Fe–Ti bonding strength has decreased to a large extent at the interface, while Ti–C strength has increased. Thus, the intraceramic bonding has reduced the magnitude of interfacial bonding. We shall see this manifests itself directly in the trends in the ideal work of adhesion as the film thickens.

Table VII shows that the total charge on interfacial Ti_1 and C_1 atoms increases significantly (0.21*e* and 0.14*e*, respectively) from the 1-ML to the 2-ML films, perhaps indicative of increased localized Ti–C bonding at the expense of interfacial bonding. The reduced Fe–Ti interactions in 2–3-ML-thick coatings also appear in the decrease in Fe-induced magnetization in Ti_1 and Ti_2 (Table VII). Accordingly, the magnetic moments of interface Fe atoms increase ($2.395\mu_B$ and $2.438\mu_B$, for 2-ML and 3-ML cases, respectively) compared to the 1-ML case. Overall, the interfacial bonding is similar in both 2-ML and 3-ML coatings; at even 2 ML, intraceramic bonding achieves full coordination.

3. Interfacial adhesion

DFT–GGA predictions of the ideal work of adhesion (W_{ad}^{ideal}) for the fully relaxed interfaces comprising up to 3-ML-thick coatings of TiC on bcc Fe are shown in Fig. 9. W_{ad}^{ideal} is defined as the energy required (per unit area) to reversibly separate an interface into two free surfaces, neglecting plastic and diffusional degrees of freedom. These dissipative processes are responsible for the fact that energy needed in an actual cleavage experiment is always considerably greater than the ideal work of adhesion.[20] Therefore, our predictions may be considered as lower bounds for the work of adhesion obtained by any cleavage experiment. Formally, W_{ad}^{ideal} is defined in terms of either the surface and interface energies relative to respective bulk materials or by the difference in total energy between the interface slab and its isolated component slabs (substrate and coating):

$$W_{ad}^{\text{ideal}} = \sigma_{1v} + \sigma_{2v} - \sigma_{12} = \frac{E^{\text{substrate}} + E^{\text{coating}} - E^{\text{interface}}}{A}, \tag{7}$$

where σ_{iv} is the surface energy per unit area of the *i*th slab, σ_{12} is the interface free energy per unit area, and $E^{\text{substrate}}$, E^{coating}, and $E^{\text{interface}}$ are the total energies of substrate (iso-

Downloaded 14 May 2003 to 128.97.45.185. Redistribution subject to AIP license or copyright, see http://ojps.aip.org/jcpo/jcpcr.jsp

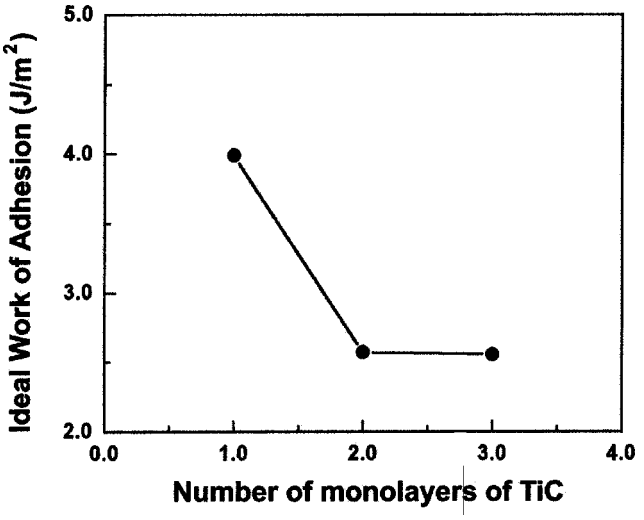

FIG. 9. Variation of ideal work of adhesion (W_{ad}^{ideal}) with coating thickness. W_{ad}^{ideal} reaches its asymptotic value (2.56 J/m^2) for a three-monolayer-thick coating of TiC.

lated), coating (isolated), and interface slabs, respectively. A is the interface area. An attractive interaction between the two crystals corresponds to $W_{ad}>0$. We have used the second identity in Eq. (7) to calculate W_{ad}^{ideal} of TiC on a Fe substrate. In order to approximately cancel the effect of lattice mismatch, we calculated the energy of the isolated coating using the same lattice vectors as for the interface, letting the atoms relax within that constraint. We find, similar to our earlier work of ZrO_2 on Ni,[42] that bonding of a single ceramic layer to an Fe substrate is considerably stronger than that for 2- or 3-ML-thick TiC coatings. The W_{ad}^{ideal} for the relaxed single monolayer coating is 3988 mJ/m^2, which drops to 2572 mJ/m^2 for 2 ML, reaching the asymptotic value of W_{ad}^{ideal} of $\sim$2550 mJ/m^2 for 3 ML. As illustrated in the electronic properties (the DOS) discussed already, the intraceramic bonding plays progressively more dominant role going from the 1-ML to 2-ML coating, with a concomitant decrease in interfacial bonding. The intraceramic bonding contribution reaches a saturation level for 3-ML coating for which the ideal work of adhesion has attained the asymptotic value.

This TiC/Fe ideal interface strength is quite respectable in size, but is below the energy required to form two surfaces of TiC(100) (3330 mJ/m^2) or of Fe(110) (4576 mJ/m^2). This implies that the heterogeneous interface will be the weak link in the material. That said, TiC may still be useful as an alternative coating for ferritic steels due to the strong covalent and metallic bonding that exists across the interface. Moreover, the high melting point, hardness, and wear-resistant properties of TiC may allow such a coating to survive harsh operating conditions.

IV. SUMMARY

In this work, we studied bulk TiC, Fe, their low index surfaces, as well as one TiC/Fe interface using a pseudopotential-based DFT–GGA method. The primary goal of the work was to assess the prospects of TiC for use as an alternative coating for steels (instead of Cr), by determining the nature of bonding at the interface and predicting the ideal work of adhesion of the TiC coating on a bcc Fe substrate. We selected an interface formed between the most stable surfaces (as determined by our calculations) of TiC and bcc Fe, viz., TiC(100)/Fe(110) interface, which shows a lattice mismatch of $\sim$2.1%. We studied up to 3-ML-thick coatings of TiC on a five-layer-thick bcc Fe substrate. We first calibrated the numerical approximations to DFT by studying the bulk properties of TiC and Fe, which were found to be in reasonable agreement with experiment. We then characterized several low-index surfaces of TiC and Fe, confirming that the surfaces retain near bulk termination, again in agreement with experiment. The stability of both bcc Fe and TiC surfaces were found to increase with packing density, with (110) most stable for bcc Fe and (100) most stable for TiC. The metal-terminated TiC(111) surface was intermediate in stability, with a mix of Ti d–C p polar covalent bonding and Ti d–d bonding. The stoichiometric TiC(100) and TiC(110) surfaces exhibited predominantly polar covalent character. Based on their surface energies, the critical stress required for crack propagation in bcc Fe was predicted to be 27% larger than that in TiC.

Our interface bonding analysis showed that the 1-ML coating utilized a mixture of covalent and metallic bonding across the interface, arising from Fe d–C p and Fe d–Ti d interactions, respectively. The equilibrium Fe–C and Fe–Ti distances for 1-ML coating were predicted to be 2.05 Å and 2.29 Å, respectively, which are close or significantly smaller than the experimental values in Fe_3C (2.02 Å), and in FeTi (2.577 Å), suggesting strong Fe–C and Fe–Ti bonding for this ultrathin coating. As the coating thickens from 1 ML to 2 ML, intraceramic bonding plays a progressively more dominant role; the interfacial Fe–Ti metallic bonding at the interface fell sharply with a concomitant increase in Ti–C polar covalent bonding. As a result, binding of a single ceramic layer to an Fe substrate was much stronger than that of 2- or 3-ML-thick TiC coatings. This is borne out by the W_{ad}^{ideal} values for these interfaces, which for a relaxed single monolayer coating was calculated to be 3988 mJ/m^2, and dropping to 2572 mJ/m^2 for the 2-ML film due to the increase in intraceramic bonding. At 3 ML, the asymptotic value of $W_{ad}^{\text{ideal}}\sim$2550 mJ/m^2 is obtained. The intraceramic bonding recovered its bulk nature by 3 ML and hence the ideal work of adhesion also attained its asymptotic value.

Our investigation of the nature of interfacial bonding and work of adhesion suggests that TiC may be useful as an alternative, environmentally friendly coating for ferritic steels, since the coating may survive harsh operating conditions owing to reasonably high adhesion at the interface.

ACKNOWLEDGMENTS

This work was supported by the Army Research Office. A Department of Defense University Research Instrumentation Program grant via the Army Research Office provided computers on which many of the calculations were per-

Downloaded 14 May 2003 to 128.97.45.185. Redistribution subject to AIP license or copyright, see http://ojps.aip.org/jcpo/jcpcr.jsp

formed. Some computations were also performed on SGI2000 machines available at NCSA at the University of Illinois.

[1] L. E. Toth, in *Transition Metal Carbides and Nitrides* (Academic Press, New York, 1971).
[2] J.-L. Calais, Adv. Phys. **26**, 847 (1977) and references therein.
[3] A. Neckel, Int. J. Quantum Chem. **23**, 1317 (1983) and references therein.
[4] B. G. Hyde, J. G. Thompson, and R. L. Withers, in *Materials Science and Technology*, edited by R. W. Cahn, P. Haasen, and E. J. Kramer, Vol. 11, edited by M. V. Swain (VCH, New York, 1993), p. 1.
[5] R. Telle, in *Materials Science and Technology*, edited by R. W. Cahn, P. Haasen, and E. J. Kramer, Vol. 11, edited by M. V. Swain (VCH, New York, 1993), p. 119.
[6] F. B. Pickering in *Materials Science and Technology*, edited by R. W. Cahn, P. Haasen, and E. J. Kramer, Vol. 7, edited by F. B. Pickering (VCH, New York, 1992), p. 335.
[7] F. Benesovsky, R. Kieffer, and P. Ettmayer, in *Encyclopedia of Chemical Technology*, edited by H. Mark, *et al.* (Wiley, New York, 1981), p. 871.
[8] K. Schwarz, CRC Crit. Rev. Solid State Mater. Sci. **13**, 11 (1987), and references therein.
[9] J. E. Truman, in *Materials Science and Technology*, edited by R. W. Cahn, P. Haasen, and E. J. Kramer, Vol. 7, edited by F. B. Pickering (VCH, New York, 1992), p. 527.
[10] *Proceedings of "Coatings for High Temperature Applications,"* edited by E. Lang (Elesevier Applied Science, London, 1983).
[11] R. Freer, in *The Physics and Chemistry of Carbides, Nitrides and Borides*, edited by R. Freer, NATO ASI Series E: Applied Sciences, Vol. 185 (Plenum, New York, 1989).
[12] L. I. Johansson, Surf. Sci. Rep. **21**, 177 (1995).
[13] V. A. Fomichev and M. A. Rumsh, J. Phys. Chem. Solids **29**, 1015 (1968).
[14] V. V. Khvostov, I. Yu. Konyashin, E. N. Shouleshov, V. G. Babaev, and M. B. Guseva, Appl. Surf. Sci. **157**, 178 (2000).
[15] M. Mizuno, I. Tanaka, and H. Adachi, Acta Mater. **46**, 1637 (1998).
[16] Z.-G. Yang and M. Enomoto, Metall. Mater. Trans. A **32**, 267 (2001).
[17] A. Christensen, E. A. A. Jarvis, and E. A. Carter, in *Chemical Dynamics in Extreme Environments*, edited by R. A. Dressler, Advanced Series in Physical Chemistry, Vol. 11, series edited by C. Y. Ng (World Scientific, Singapore, 2001), pp. 490–546.
[18] J.-G. Li, J. Am. Ceram. Soc. **75**, 3118 (1992).
[19] F. Ernst, Mater. Sci. Eng., R. **14**, 97 (1995).
[20] M. W. Finnis, J. Phys.: Condens. Matter **8**, 5811 (1996).
[21] *ASM Engineering Materials Reference Book* (ASM International, Metals Park, OH, 1989).
[22] *Smithells Metals Reference Book*, edited by E. A. Brandes and G. B. Book (Butterworth-Heinemann, Oxford, 1998).
[23] *CRC Materials Science and Engineering Handbook*, edited by J. F. Shackleford, W. Alexander, and J. S. Park (CRC, Boca Raton, 1994).
[24] I. Barin, O. Knacke, and O. Kubaschewski, *Thermochemical Properties of Inorganic Substances* (Springer, Berlin, 1989).
[25] H. Adachi, M. Tsukada, and C. Satoko, J. Phys. Soc. Jpn. **45**, 875 (1978).
[26] D. E. Ellis and G. S. Painter, Phys. Rev. B **2**, 2887 (1970).
[27] D. D. Koelling and G. O. Arbman, J. Phys. F: Met. Phys. **5**, 2041 (1975).
[28] O. K. Andersen, O. Jepsen, and M. Sob, in *Electronic Band Structure and its Applications*, edited by M. Yussouff, *Springer Lecture Notes in Physics* Vol. 283 (Springer, Berlin, 1987), p. 1.
[29] O. K. Andersen, Phys. Rev. B **12**, 3060 (1975).
[30] A. Dominguez-Rodriguez and A. H. Heuer, in *Surfaces and Interfaces of Ceramic Materials*, edited by L. C. Dufour *et al.* (Kluwer, Dordrecht, 1989), p. 761.
[31] S. Zaima, Y. Shibata, H. Adachi, C. Oshima, S. Otani, M. Aono, and Y. Ishizawa, Surf. Sci. **157**, 380 (1985).
[32] D. L. Price and B. R. Cooper, Phys. Rev. B **39**, 4945 (1989).
[33] C. Oshima, M. Aono, T. Tanaka, S. Kawai, S. Zaima, and Y. Shibata, Surf. Sci. **102**, 312 (1981).
[34] A. Fujimori, F. Minami, and N. Tsuda, Surf. Sci. **121**, 199 (1982).
[35] E. Wimmer, A. Neckel, and A. J. Freeman, Phys. Rev. **B31**, 2370 (1985).
[36] D. L. Price, J. M. Wills, and B. R. Cooper, Phys. Rev. Lett. **77**, 3375 (1996).
[37] K. Kobayashi, Jpn. J. Appl. Phys., Part 1 **39**, 4311 (2000).
[38] F. R. de Boer, R. Boom, W. C. M. Mattens, A. R. Miedema, and A. K. Niessen, *Cohesion in Metals* (North-Holland, New York, 1988).
[39] W. R. Tyson and W. A. Miller, Surf. Sci. **62**, 267 (1977).
[40] L. Vitos, A. V. Ruban, H. L. Skriver, and J. Kollar, Surf. Sci. **411**, 186 (1998).
[41] H. L. Skriver and N. M. Rosengaard, Phys. Rev. B **46**, 7157 (1992).
[42] A. Christensen and E. A. Carter, J. Chem. Phys. **114**, 5816 (2001).
[43] E. A. A. Jarvis, A. Christensen, and E. A. Carter, Surf. Sci. **487**, 55 (2001).
[44] E. A. A. Jarvis and E. A. Carter, Comput. Sci. Eng. **4**, 33 (2002).
[45] D. R. Jennison, C. Verdozzi, P. A. Schultz, and M. P. Sears, Phys. Rev. B **59**, R15605 (1999).
[46] D. R. Jennison and A. Bogicevic, Faraday Discuss. **114**, 45 (1999).
[47] D. R. Jennison and A. Bogicevic, Surf. Sci. **464**, 108 (2000).
[48] S. V. Dudiy, J. Hartford, and B. I. Lundqvist, Phys. Rev. Lett. **85**, 1898 (2000).
[49] S. V. Dudiy and B. I. Lundqvist, Phys. Rev. B **64**, 045403 (2001).
[50] S. V. Dudiy, Surf. Sci. **497**, 171 (2002).
[51] M. Christensen, S. V. Dudiy, and G. Wahnstrom, Phys. Rev. B **65**, 045408 (2002).
[52] R. Benedek, A. Alavi, D. N. Seidman, L. H. Yang, D. A. Muller, and C. Woodward, Phys. Rev. Lett. **84**, 3362 (2000).
[53] Y. F. Zhukovskii, A. Kotomin, P. W. M. Jacobs, and A. M. Stoneham, Phys. Rev. Lett. **84**, 1256 (2000).
[54] R. Benedek, D. N. Seidman, M. Minkoff, L. H. Yang, and A. Alavi, Phys. Rev. B **60**, 16094 (1999).
[55] W. Zhang and J. R. Smith, Phys. Rev. B **61**, 16883 (2000).
[56] A. M. Stoneham, M. M. D. Ramos, and A. P. Sutton, Philos. Mag. A **67**, 2221 (1993).
[57] J. P. Perdew, J. A. Chevary, S. H. Vosko, K. A. Jackson, M. R. Pederson, and C. Fiolhais, Phys. Rev. B **46**, 6671 (1992); J. P. Perdew, K. Burke, and Y. Wang, *ibid.* **54**, 16 533 (1996).
[58] A. Christensen and E. A. Carter, Phys. Rev. B **58**, 8050 (1998).
[59] J. P. Perdew and A. Zunger, Phys. Rev. B **23**, 6512 (1981).
[60] G. Kresse and J. Furthmüller, Comput. Mater. Sci. **6**, 15 (1996).
[61] G. Kresse and J. Furthmüller, Phys. Rev. B **54**, 11169 (1996).
[62] D. Vanderbilt, Phys. Rev. B **41**, 7892 (1990); G. Kresse and J. Hafner, J. Phys.: Condens. Matter **6**, 8245 (1994).
[63] N. D. Mermin, Phys. Rev. **137**, 1441 (1965).
[64] L. Kleinman and D. M. Bylander, Phys. Rev. Lett. **48**, 1425 (1982).
[65] A. M. Rappe, K. M. Rabe, E. Kaxiras, and J. D. Joannopoulos, Phys. Rev. B **41**, 1227 (1990).
[66] D. Das, in *Lectures on Methods of Electronic Structure Calculations*, edited by V. Kumar, O. K. Andersen, and A. Mookerjee (World Scientific, Scientific, 1994), p. 1.
[67] M. Methfessel and A. T. Paxton, Phys. Rev. B **40**, 3616 (1989).
[68] P. Villars and L. D. Calvert, *Pearson's Handbook of Crystallographics Data on Intermetallics* (ASM, Metals Park, OH, 1991).
[69] V. L. Moruzzi, J. F. Janak, and A. R. Williams, *Calculated Electronic Properties of Metals* (Pergamon, New York, 1978).
[70] E. G. Moroni, G. Kresse, J. Hafner, and J. Furthmüller, Phys. Rev. B **56**, 15629 (1997).
[71] F. D. Murnaghan, Proc. Natl. Acad. Sci. U.S.A. **30**, 2344 (1944).
[72] J. P. Perdew and A. Zunger, Phys. Rev. B **23**, 5048 (1981).
[73] M. Aono and R. Souda, Jpn. J. Appl. Phys., Part 1 **24**, 1249 (1985).
[74] W. D. Callister, Jr., *Materials Science and Engineering* (Wiley, New York, 2000), p. 193.

Downloaded 14 May 2003 to 128.97.45.185. Redistribution subject to AIP license or copyright, see http://ojps.aip.org/jcpo/jcpcr.jsp